



UNIVERSITÀ DEGLI STUDI DI PADOVA

DEPARTMENT OF CIVIL, ENVIRONMENTAL AND ARCHITECTURAL
ENGINEERING

Corso di Laurea in Magistrale in Mathematical Engineering

Tesi di Laurea Magistrale

**Computational Fluid-Dynamic
Analysis of the Particle Size Effects
on the Breakage of Light Ductile
Aggregates**

Relatori

Chia.mo Prof. Paolo Peruzzo

Chia.ma Prof.ssa Laura Maria Stancanelli

Candidato

Nicolò Cappello

2023618

October 2025

Contents

1	introduction	3
2	Methods and Models	7
2.1	Hydrodynamics	7
2.2	Discrete Phase Model (DPM)	15
3	Results and Discussion	21
3.1	Hydrodynamics	21
A	Some Background	35
A.1	Hydrodynamics	35
	Bibliography	39

Chapter 1

introduction

Environmental DNA (eDNA) refers to genetic material continuously shed by organisms into their surrounding environment in the form of free fragments, cells, tissues or feces. Over the last decade, eDNA analysis has emerged as a powerful and effective biomonitoring tool for assessing biodiversity in aquatic ecosystems. Unlike traditional sampling methods, which are often labor-intensive and species-specific, eDNA detection offers a rapid, non-invasive approach capable of capturing signals across a broad taxonomic range [1]. However, the reliability of eDNA as a monitoring technique depends critically on understanding the physical and biochemical processes that govern its persistence, transport, and detectability. After release into lotic environments such as rivers or streams, eDNA is subjected to advection, turbulent mixing, particle fragmentation, adsorption and degradation. These combined processes lead to spatial and temporal variability between the source signal and the measurable concentration downstream, introducing uncertainty into ecological interpretation. In particular, flow velocity and turbulence play a decisive role: they can keep eDNA particles in suspension, enhance their mixing, or conversely accelerate their fragmentation and degradation. To investigate these mechanisms under controlled conditions, Dercksen et al. [2] employed a rectangular cross-section annular flume in which the top lid and bottom bed rotate in opposite directions. This configuration minimizes secondary circulations typical of curved channels and allows for long-duration degradation and transport experiments under well-defined flow velocities. Their results highlighted the strong dependence of eDNA detectability on hydrodynamic forcing, emphasizing the importance of turbulent shear stresses in modulating particle fate.

Figure 1.1 displays the annular flume experimental setup and the different procedural phases followed by the researchers. The utilized eDNA source was wildtype zebrafish rearing water, spread across 50 tanks of 10 L each. 60 L of rearing water was collected and added to the flume 15 min before initiation of each experiment. The flume was rotated at low speed in order to uniformly distribute the eDNA concentration throughout the tank, after which the experiment was started.

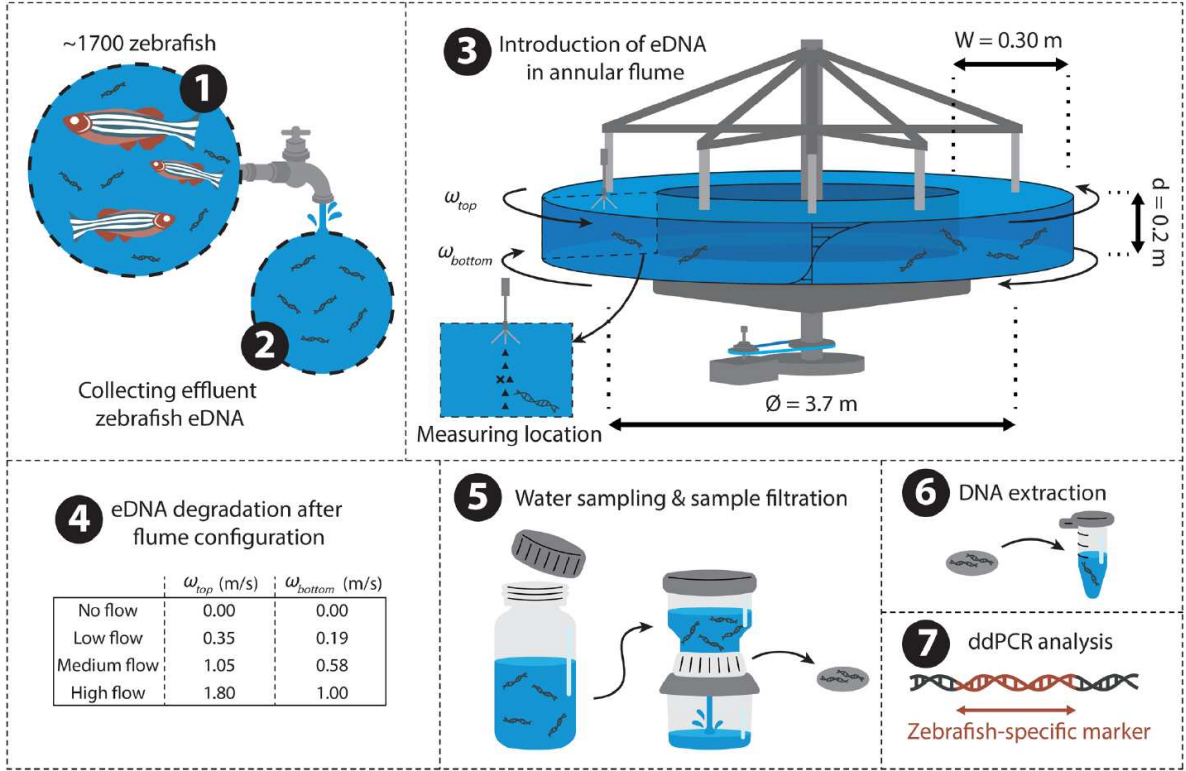


Figure 1.1: Experimental setup implemented by Dercksen et al. This figure is taken from [2]

Four experiments were performed each one lasting for 7 days. Water sub-samples were acquired at six longitudinally evenly spaced locations in the annular flume, combined, filtered and analyzed in order to detect eDNA concentration. The total number of samples collected (for each experiment) was 30, acquired at different time lags since the initiation of the experiment. Thus the eDNA concentration detected at varying elapsed time was assessed.

The present dissertation extends this line of research by employing computational fluid dynamics (CFD) simulations of the same toroidal flume configuration. The modeled and analyzed domain is scaled by a factor 10 with respect to the laboratory apparatus (by keeping invariated the proportions), in order to gain the possibility of reaching higher fineness mesh levels. By replicating the laboratory apparatus in Fluent, the numerical study aims at resolving the detailed turbulence structures within the flow and assess their influence on particle dispersion and rupture, at varying particle size. Particular emphasis is placed on quantifying temporal and spatial correlations, energy spectra, and integral length scales in different regions of the flume, with the overall goal of providing a numerical and computational framework that complements experimental observations. Ultimately, this approach bridges controlled laboratory studies and hydrodynamic modeling, contributing

to a more mechanistic understanding of eDNA dynamics in turbulent aquatic environments.

Chapter 2

Methods and Models

2.1 Hydrodynamics

The first part of this dissertation has regarded the hydrodynamical analysis of the rotating tank. The geometry of the system and the prescribed boundary conditions provide a very peculiar fluid motion inside the flume. Figure 2.1 shows the fluid domain along with the boundary conditions being enforced.

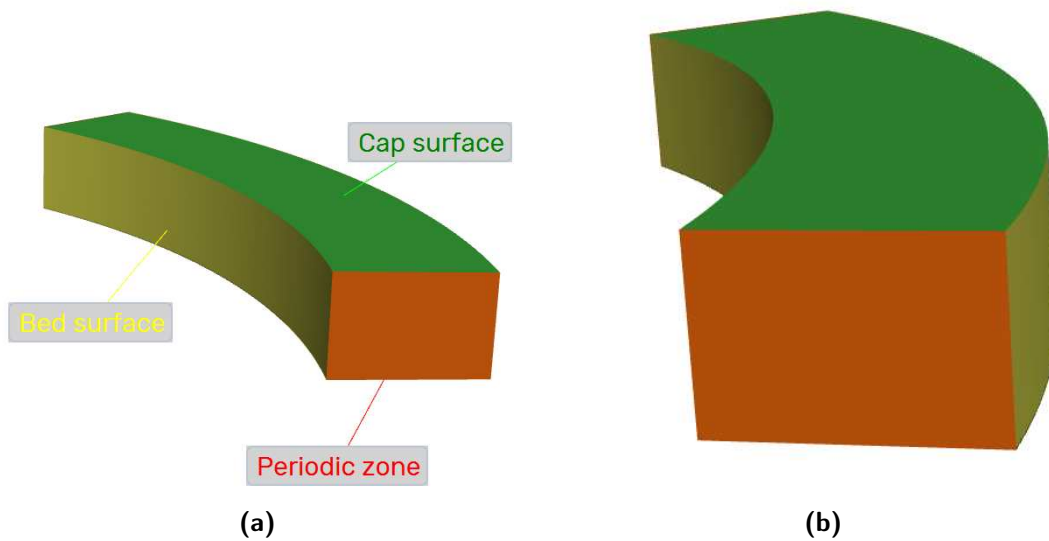


Figure 2.1: Simulated domain with named boundaries.

Notice that, in order to achieve a good mesh resolution (which is a fundamental point, in particular for what concerns the LES simulations), just one eighth of the full toroidal flume has been simulated, and periodic conditions has been set onto the two cross-sectional surfaces. The fluid domain consists of a rectangular-cross-sectional annular chunk, characterized by a (3×2) cm² cross-section. To define the

boundary conditions we shall name first the boundary surfaces enclosing the fluid volume. Therefore, we distinguish:

- The *cap*, i.e. the top ring-shaped surface enclosing the domain;
- The *bed*, namely the horseshoe shaped surface consituted of the bottom plus the two vertical boundary surfaces;
- The periodic interface, which is indeed composed by the two cross-sectional rectangular surfaces.

The inner radius of the flume equals 17 cm, whereas the outer radius amounts to 20 cm.

Having identified the domain boundaries, then the boundary conditions prescribed for the system are:

Bed: moving wall boundary type, no slip adherence condition, imposed rotational speed $|v_b| = 1.0 \text{ m/s}$ referred to the mid radius.

Cap: moving wall boundary type, no slip adherence condition, imposed rotational speed $|v_c| = 1.8 \text{ m/s}$ referred to the mid radius, in the opposite direction with respect to the bed.

Period interface: rotationally periodic boundaries.

Domain volume: fluid type domain, with operating fluid being liquid water: $\rho = 998.2 \text{ Kg/m}^3$, $\mu = 0.001003 \text{ Kg/(ms)}$.

The mesh employed to tackle the fluid-dynamic solution of the system is a *polyhedral* mesh, generated with Ansys Fluent Meshing. The mesh is shown in Figure 2.2. The polyhedral topology has been chosen because it is suitable to fill the space and to reach pretty high levels of fineness by keeping the total number of cells (and nodes) adequately small. As it is shown in Figure 2.2, the cell density has been increased in correspondence of the expected hot-spot zones in the regards of the turbulence production, namely close to the intersection edges between bed and cap. In these zones, the highest velocity gradients and shear production are expected to take place. Moreover, a highly thin inflation layer has been attached to the wall surfaces in order to guarantee the wall-resolved condition. The hydrodynamics stage of the work has been carried out in two subsequent steps:

1. A first run of (steady) RANS, aiming at testing the validity of the employed mesh and the wall-resolved condition, assessing flow-averaged quantities, and also obtaining an effective flow condition to be exploited as initial condition in the subsequent LES phase.

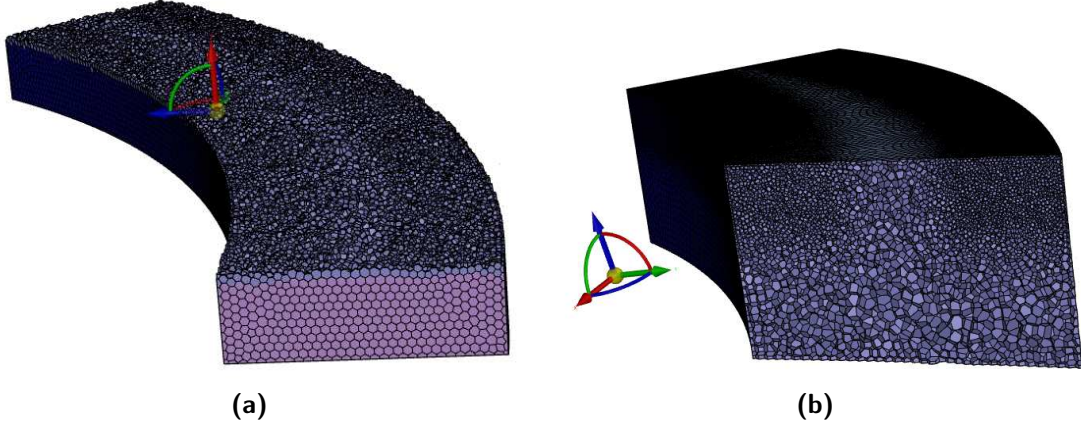


Figure 2.2: Employed mesh. Left panel shows a cut of the meshes domain with a plane orthogonal to the z axis. Right panel show the elements distribution onto a cross-section of the domain, highlighting the increasing mesh fineness towards the upper-outer edge.

2. A wall-resolved LES (WRLES) run, allowing for a deep exploration of the turbulence structures inside the tank, with the assessment of the temporal and spatial correlation coefficients (hence characteristic time and length-scales of the system), velocity and energy spectra and qualitative visualization of the evolution of coherent structures.

RANS simulation

For the steady RANS simulation the $k\omega - \text{SST}$ turbulence model has been used in order to solve the mean flow equations. To account for the relatively strong curvature of the streamlines, as well as corner flow effects, introduced in the dynamics of the system by the rectangular shape of the flume, the $k\omega - \text{SST}$ model has been powered up by *curvature correction* and *corner flow correction*. The steady RANS simulation lasted for a period sufficient to obtain an appropriate convergence of the monitored integral quantities. The three integral variables monitored to judge convergence are:

- The *volume flow rate* across the middle cross-section of the system;
- The integral-mean valued of the *wall shear stress* averaged onto the cap surface;
- The values (and possible relative departures) of the area-weighted-average value of the *turbulent dissipation rate* ε on three different cross-sections along with the volume-averaged value on the whole domain.

From the RANS simulations useful mean quantities characterizing the flow field have been extracted, such as the distributions of the y^+ (defined as $y^+ = yu_\tau/\nu$ where y is the orthogonal distance from the wall and $u_\tau = \sqrt{\tau_w/\rho}$ is the so-called friction-velocity) across the bed and cap surfaces, which provide a fundamental indication about the degree of wall-resolution. Beside the y^+ , the distributions of the wall shear stress was detected, showing the behaviour of the shear stresses at the domain boundaries and giving insights about the more loaded wall zones. In addition to the wall behaviour, from the RANS run the outlines of the mean-tangential velocity profiles at different constant-radius vertical lines in a predefined cross-section (the cross-section with constant angular coordinate equal to the mid value of the total angle spanned by the domain) have been assessed, showing how the velocity profiles (namely the tangential velocity gradients) changes as the radius of the vertical line at which we evaluate them increases from the inner ($r = 0.170$ m) to the outer domain radius ($r = 0.200$ m). Another precious information yielded by the RANS processing is the volume-averaged value of the *turbulent energy dissipation rate* $\bar{\varepsilon}$; this value turns out to be very effective because it is used to roughly estimate the Kolmogorov length and timescale (η , τ_η) characterizing the flow field. The information content offered by the Kolmogorov scales constitutes a twofold utility:

1. On the one hand, knowing the length scale η allows one to determine in advance which will be the fraction of the turbulent kinetic energy being resolved by the mesh. Indeed, the more the characteristic size of the mesh approaches the value of η the higher the resolved energy fraction will be (the limit being the DNS case, where the size of each mesh-cell is comparable, if not smaller than the Kolmogorov length scale).
2. On the other hand, the Kolmogorov timescale τ_η provides an upper limit for the time-step-size to be utilized throughout the (time-dependent) LES run. Indeed, adopting a time-step-size bigger than τ_η would be conceptually wrong, since the dynamics of the smallest resolved eddies would not be adequately captured.

LES simulation

The final converged solution of the RANS simulation has been fed to the solver as starting solution for the subsequent LES run. This subtlety is actually very important in the CFD practice, in that the solver needs a realistic initial guess of the flow field in order to start addressing the large eddy dynamics. The Large Eddy Simulation's goal is twofold:

1. Get useful important information about the turbulence structure inside the tank.
2. Recreate a base realistic turbulent motion to feed with the particles.

The turbulence analysis has been devoted to the assessment of both the spatial and temporal correlation coefficients. In general, the *two-point, two-times correlation function* between fluctuating components i and j of the velocity is defined as:

$$R_{ij} = \langle u_i(\mathbf{x}_1, t_1) u_j(\mathbf{x}_2, t_2) \rangle \quad (2.1)$$

where, generally speaking, $\langle \cdot \rangle$ is either an ensemble mean or a temporal mean (see [...]). By letting $\mathbf{x}_1 \equiv \mathbf{x}$, $\mathbf{x}_2 \equiv \mathbf{x} + \mathbf{r}$, $t_1 \equiv t$, $t_2 \equiv t + \tau$ we can rewrite the correlation function as

$$R_{ij}(\mathbf{x}, t, \mathbf{r}, \tau) = \langle u_i(\mathbf{x}, t) u_j(\mathbf{x} + \mathbf{r}, t + \tau) \rangle \quad (2.2)$$

From the correlation function one can define the *correlation coefficient*:

$$\rho_{ij}(\mathbf{x}, t, \mathbf{r}, \tau) = \frac{R_{ij}(\mathbf{x}, t, \mathbf{r}, \tau)}{\sqrt{\langle u_i^2(\mathbf{x}, t) \rangle \langle u_j^2(\mathbf{x} + \mathbf{r}, t + \tau) \rangle}} \quad (2.3)$$

so that ρ can attain values between -1 (perfect anticorrelation) and 1 (perfect correlation). Setting $\mathbf{r} = \mathbf{0}$ we get the (one-point) temporal correlation function (and coefficient), defined as

$$R_{ij}(\mathbf{x}, t, \tau) = \langle u_i(\mathbf{x}, t) u_j(\mathbf{x}, t + \tau) \rangle, \quad \rho_{ij}(\mathbf{x}, t, \tau) = \frac{R_{ij}(\mathbf{x}, t, \tau)}{\sqrt{\langle u_i^2(\mathbf{x}, t) u_j^2(\mathbf{x}, t + \tau) \rangle}} \quad (2.4)$$

Conversely, by setting in (2.1) $\tau = 0$, one gets the two-point (one-time) correlation function and coefficient, defined as:

$$R_{ij}(\mathbf{x}, \mathbf{r}, t) = \langle u_i(\mathbf{x}, t) u_j(\mathbf{x} + \mathbf{r}, t) \rangle, \quad \rho_{ij}(\mathbf{x}, \mathbf{r}, t) = \frac{R_{ij}(\mathbf{x}, \mathbf{r}, t)}{\sqrt{\langle u_i^2(\mathbf{x}, t) u_j^2(\mathbf{x} + \mathbf{r}, t) \rangle}} \quad (2.5)$$

Spatial and temporal correlation coefficients give precious insights about the spatial, respectively temporal, structure of turbulent eddies, namely, how far in space and time do turbulent fluctuations stay correlated to each other. Two remarks are worth being made:

- In the case of *stationary turbulence*, the statistics do not depend on the time origin at which they are computed, hence in such a case one has:

$$R_{ij}(\mathbf{x}, \mathbf{r}, t, \tau) \equiv R_{ij}(\mathbf{x}, \mathbf{r}, \tau) \quad (2.6)$$

This happens, for instance, in turbulent flows that persist for sufficiently long times with the same boundary conditions (like the objective of this dissertation).

- In the case of *spatially homogeneous turbulence*, the statistics are independent of the base point \mathbf{x} at which they are computed. Therefore, in such a scenario one would have:

$$R_{ij}(\mathbf{x}, \mathbf{r}, t, \tau) \equiv R_{ij}(\mathbf{r}, t, \tau) \quad (2.7)$$

Unfortunately the studied turbulent flow is far from being homogeneous, due to the major influence of the walls on the flow field, the intense curvature of the streamlines induced by the curvature of the tank itself and the rectangular cross-section of the flume that cause corner-flow effects on the planes orthogonal to the stream direction.

Due to the toroidal (hence axisymmetric) shape of the domain, we will use when convenient to cylindrical coordinates (r, θ, z) , where θ constitutes the toroidal (or tangential, or streamwise) direction and for our domain it attains values $\theta \in [0.0, 45.0]$ deg, r represents the radial direction, and takes values $r \in [0.17, 0.20]$ m, and finally z is the height coordinate with values $z \in [0.0, 0.020]$ m. Figure ?? represents the computational setup implemented to assess the correlation coefficients. As it can be seen in the Figure, the mid-angular-coordinate cross-section has been created (the cross section constituted by the equation $\theta = 22.5$ deg). Onto that rectangular surface 7 base points have been defined, whose (cylindrical) coordinates are synthesized in Table 2.1.

Table 2.1: Coordinates of the centers of the rakes.

Point name	r [m]	θ [deg]	z [m]
upper-outer	0.1985	22.5	0.019
upper-inner	0.1715	22.5	0.019
mid-outer	0.1955	22.5	0.010
mid-inner	0.1755	22.5	0.010
lower-outer	0.1985	22.5	0.001
lower-inner	0.1715	22.5	0.001
center	0.1850	22.5	0.010

Figure 2.3 shows the modeling setup described above implemented for the assessment of the correlations.

For each of these 7 base points \mathbf{x}_0 the temporal autocorrelation coefficients $\rho_{ii}(\mathbf{x}_0, \tau)$ $i = 1, 2, 3$ have been computed and the respective integral time-scales assessed. Then, at the same base points, we evaluated also the spatial auto and cross-correlation coefficients, namely $\rho_{ab}(\mathbf{x}_0, \Delta \mathbf{x})$ with $a, b = r, \theta, z$, focusing in particular on the toroidal (streamwise) correlation, that is setting $\Delta \mathbf{x} = (\Delta r, \Delta \theta, \Delta z) \equiv (0, \Delta \theta, 0)$. In order to inspect toroidal correlations, toroidal rakes of points have

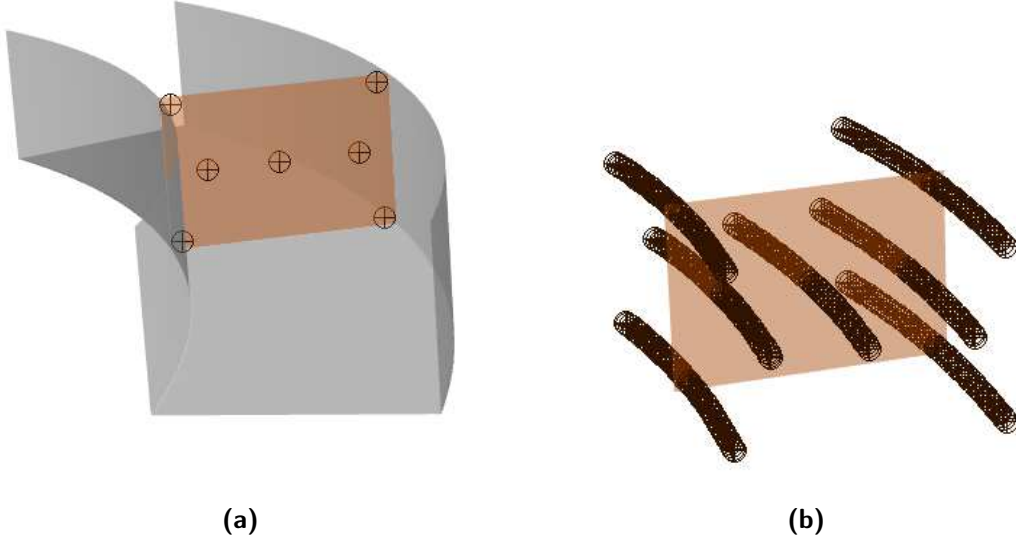


Figure 2.3: Computational setup to assess spatial correlation coefficients. Left panel displays the bed wall, along with centers of the toroidal rakes on their lying cross-section. Right panel reports the 7 toroidal rakes, symmetric with respect to the cross-section.

been created such that, starting at each of the base points \mathbf{x}_0 , 30 points have been added in both the $\pm\theta$ directions ($2K + 1 = 61$ points per rake) by keeping the values of r, z constantly equal to those of the respective base point, and by letting a $\Delta\theta = 0.004$ rad between each couple of nodes. Then the three velocity components u_r, u_θ, u_z have been dumped at each time step for all of the nodes of each rake, gathering this way the dataset from which to extract correlations. An important remark is worth being made at this point: in theory, the integral scale is defined as the integral of the correlation function up to infinite lag. In practice, however, the correlation functions obtained from LES point-surface signals exhibit long noisy tails at large time lags, which introduce spurious oscillations and can even yield unphysical negative values of the integral. To avoid this issue, we adopted the common practical criterion of truncating the integration at the *first zero crossing* of the correlation coefficient (i.e., the first time lag τ_0 for which $\rho_{ii}(\tau_0) \leq 0$). This provides a robust estimate of the dominant decorrelation time of the turbulence while avoiding contamination from poorly converged long-lag statistics. In addition, for some rakes the evaluated toroidal (spatial) correlation coefficient turned out not to cross the $\rho = 0$ axis, probably due to the limited length of the rake compared to the relative large eddies-structure in that zone. For those non-crossing correlation, the reported integral scale is therefore just a lower bound.

Finally, a spectral analysis of turbulence has been carried out. The procedural steps employed to perform spectral analysis can be organized as follows:

1. The first step is of course recording the raw time series of the three velocity components u_x , u_y and u_z (or u_r , u_θ and u_z) at each of the base points. Actually, for the purposes of spectral post-processing, it is very important that the time series recording be performed at a *uniform sampling frequency*. This means, if the velocity components instant values are dumped at each solver time step, the time stepping be uniform.
2. The gathered time signals needs to be detrended (in some circumstance due to numerical errors or to a time signal not still perfectly statistically stationary the time series may present a slight linear trend) and zero-mean (so as to get the true fluctuation $u'_i(\mathbf{x}, t) = u_i(\mathbf{x}, t) - U_i(\mathbf{x})$).
3. Here comes in the fundamental step: the turbulent velocity time series were analyzed using Welch's method to estimate power spectral densities. Each record was divided into overlapping segments (50% overlap), windowed with a Hann window to reduce spectral leakage, and Fourier transformed. The squared magnitudes were normalized and averaged across all segments. This approach reduces the variance of spectral estimates compared to a single Fourier transform, at the expense of reduced frequency resolution. The method is standard in turbulence analysis, ensuring statistically converged spectra even from relatively short records.
4. Finally, exploiting Taylor's frozen flux hypothesis the frequency domain (PSD) was mapped into the wavenumber space to obtain the turbulent energy spectrum for each of the velocity components:

$$k = \frac{2\pi f}{U_c}, \quad E_{ii}(k) = \frac{U_c}{2\pi} \text{PSD}_{ii}(f) \quad (2.8)$$

where f is the fluctuating frequency, U_c is the local convective velocity (usually the mean streamwise velocity component), k is the (scalar) wavenumber, PSD_{ii} is the Power Spectral Density and E_{ii} the turbulent energy spectrum relative to the i velocity component.

5. Once the energy spectra for all the velocity components are computed, one can finally assess the total turbulent kinetic energy spectrum, which is given by:

$$E_{\text{TKE}}(k) = \frac{1}{2}(E_{11}(k) + E_{22}(k) + E_{33}(k)) \quad (2.9)$$

This spectrum in homogeneous isotropic turbulence fulfills the famous Kolmogorov $-5/3$ law.

2.2 Discrete Phase Model (DPM)

The second part of the work has focused on particle tracking and trajectory analysis. The main objective of this part was to study the Lagrangian dynamics of clusters of particles having different size injected into the fluid flow. In order to address this task, the DPM (Discrete Phase Modeling) model of Ansys Fluent has been employed allowing for the temporal integration of the Lagrangian equations of motions of each particle. The DPM model in Ansys Fluent implements an Euler-Lagrange approach to the numerical simulation of multiphase flows. In this approach, the fluid phase (often referred to as the *gas phase*) is considered as a continuum, hence governed by the Navier-Stokes equations, while the discrete phase, which has of course to be immiscible with the fluid, is treated as a discrete system of aggregates (called *parcels*) each of which is tracked in space and time by integrating the associated Lagrangian equations of motions. Each parcels is allowed to exchange heat, momentum and mass with the fluid phase. The equation of motion governing the trajectory of each particle and integrated by the solver is written as:

$$m_p \frac{d}{dt} \mathbf{u}_p = m_p \frac{\mathbf{u} - \mathbf{u}_p}{\tau_r} + m_p \mathbf{g} \frac{\rho_p - \rho}{\rho_p} + \mathbf{F} \quad (2.10)$$

where m_p is the mass of the particle, \mathbf{u}_p and \mathbf{u} are the particle and local fluid velocity at the particle center of mass, respectively, and ρ_p and ρ are the particle and fluid phase densities, respectively. Finally, τ_r is the particle relaxation time, which according to [...] is defined as:

$$\tau_r = \frac{\rho_p d_p^2}{18\mu} \frac{24}{C_d \text{Re}}$$

Here d_p is the particle diameter, μ is the fluid dynamic viscosity and Re is the Reynolds number referred to the relative particle velocity, namely

$$\text{Re} = \frac{d_p \|\mathbf{u} - \mathbf{u}_p\|_2}{\nu}$$

with $\nu = \mu/\rho$ the kinematic viscosity of the fluid phase.

Notice that the first term at the right-hand-side of Equation (2.10) represents the drag force acting on the particle, whereas the second term amounts to the gravitational action which the parcel is subject to. The last term at the RHS accounts for all the other external forces which, depending on the physical nature of the problem can act on the immersed body. Among all the forces that can be incorporated in the \mathbf{F} term, the two contributions that turns out to be important for the simulation of eDNA particles in the tank are the *virtual mass force* and the *pressure gradient force*. The first is the force required to accelerate the fluid

surrounding the parcel. The formula proposed by Ansys Fluent to compute the added mass force is:

$$\mathbf{F}_{\text{vm}} = C_{\text{vm}} m_p \frac{\rho}{\rho_p} \left(\mathbf{u}_p \cdot \nabla \mathbf{u} - \frac{d\mathbf{u}_p}{dt} \right)$$

where $C_{\text{vm}} = 0.5$ is a scalar coefficient. In contrast, the force due to the pressure gradient acting in the fluid motion is computed as:

$$\mathbf{F}_{\text{pg}} = m_p \frac{\rho}{\rho_p} \mathbf{u} \cdot \nabla \mathbf{u}$$

These two forces are negligible when the particles of the dispersed phase have a much higher density than the carrier phase, and become more important as the density of the discrete phase approaches that of the fluid (Ansys Fluent suggests to call them into play when the ratio $\rho/\rho_p > 0.1$). This underlines why these two forces are predominant in the present analysis, since the eDNA has a density ratio with respect to water which is so close to unity (0.9883). Therefore, it is also worth pointing out that for the analyses carried out in the present work, the buoyant effect $m_p \mathbf{g}(\rho_p - \rho)/\rho_p$ is negligible and hence the solendimensionless group which dominates the dynamics of the particles is the *Stokes number*, defined as

$$\text{St} = \frac{\tau_r}{\tau_\eta} \tag{2.11}$$

where τ_r is the particle relaxation time, and τ_η is the Kolmogorov time scale. In order to predict the particles trajectory, Ansys Fluent integrates in time the following coupled system of ordinary differential equations (ODEs):

$$\begin{cases} \frac{d\mathbf{x}_p}{dt} = \mathbf{u}_p \\ \frac{d\mathbf{u}_p}{dt} = \frac{\mathbf{u} - \mathbf{u}_p}{\tau_r} + \mathbf{a} \end{cases} \tag{2.12}$$

where \mathbf{a} accounts for all the acceleration terms different from the drag contribution (gravity force, pressure gradient force, forces of thermal origin, etc). In order to solve the above system of ODEs, the solver automatically switches between a lower order unconditionally stable scheme (an implicit Euler scheme) and an higher order scheme (a Trapezoidal method), based on the accuracy to be achieved. During runtime, based on how far from hydrodynamical equilibrium the particle is, the solver automatically choose what scheme to pick.

The interaction between the two phases can be uncoupled or coupled. The uncoupled scenario assumes that the discrete phase particles are passively subjected to the fluid phase dynamics, without causing any counter-effect on it. Vice versa, it is possible to account for the mutual interaction between the fluid and the dispersed

phase; the mass, heat and momentum exchanges between each particle and the fluid are computed at each time step and are converted into mass, heat and momentum sources in each subsequent calculation of the continuous phase flow field. In the present work two-way coupling is adopted, in such a way that from the knowledge of the momentum sources in the fluid phase it is possible to compute the corresponding total forces exerted from the fluid onto the particles. This would not be possible adopting an uncoupled solution strategy. Moreover, the same time step size is used for the continuous phase equations and for the particles motion equations. Thus, at each time step the fluid phase equations are solved, the particles are tracked, and all the parcels variables necessary to investigate the discrete phase dynamics are dumped into text files. Then, once the simulation is completed, the postprocessing of the particles data is performed in Matlab, which consists basically in two phases. Firstly, from the acquired data set, a statistical analysis on the stresses experienced by the particle cluster is carried out. Then, from the statistical assessment of the stresses, an analysis and synthesis of the breakage behaviour of the clusters has been conducted. Two different stresses are taken into account in the present analysis: the turbulent shear stress σ_ε , i.e. the stress due to turbulent shear motions computed as:

$$\sigma_\varepsilon(\mathbf{x}, t) = C_\varepsilon \mu \sqrt{\frac{\varepsilon(\mathbf{x}, t)}{\nu}} \quad (2.13)$$

where C_ε is a scalar constant which assumes value $\sqrt{2/15}$ in the case of homogeneous isotropic turbulence and is expected to attain a larger value in the more general inhomogeneous scenario and ε is the turbulence energy dissipation rate $\varepsilon = 2\nu s_{ij}s_{ij}$, with $s_{ij} = 1/2(\partial_i u_j + \partial_j u_i)$. The other stresses accounted for is the drag stress σ_{St} , i.e. the ratio between the drag force acting on the particle and the particle surface area computed as

$$\sigma_{St} = 3\mu \frac{\|\mathbf{u} - \mathbf{u}_p\|_2}{D_p} \quad (2.14)$$

Then, according to Kusters [5] the two stress contributions have to be added up linearly to obtain the total stress acting on the parcel, which results in:

$$\sigma_{tot} = \sigma_\varepsilon + \sigma_{St}$$

Probability density functions for both σ_ε , σ_{St} and σ_{tot} are extracted for each diameter-family of particles, allowing one to see how the stresses are experimented differently as the diameter (hence the Stokes number) varies.

Once the stress statistics are assessed, the breakage analysis of the aggregates can be performed. In the present work two scenarios are explored: first, the brittle rupture is considered. Here, the breakup criterion establishes that, as soon as the total stress acting on the particle exceed a prefixed strength threshold the particle itself undergoes instantaneous breakage. Second, the ductile rupture is inspected. There, it is not the stress itself to trigger the breakage, but instead the

cumulated strain energy when the particle experiences a stress above its mechanical resistance. When the accumulated energy exceeds a threshold value, the particle breaks intantaneously up.

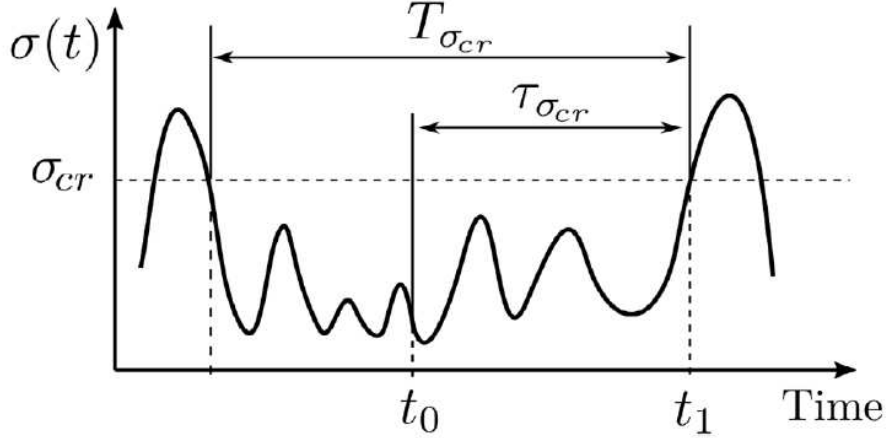


Figure 2.4: Graphical definition of the first exit time and diving time. The particle is released at time t_0 . The total stress it experiences at t_0 must be below the threshold σ_{cr} .

Following the operative procedure outlined in [4], to assess the breakup rates of the particle families the procedure is the following: the parcels are released at randomized initial positions in the fluid domain at time t_0 . Their trajectory is then computed for a time interval sufficiently long to allow experiencing the entire flow field. Then, once decided a value of mechanical strength threshold σ_{cr} , for each particle, we assess the time interval $\tau_{\sigma_{cr}}$ i.e., the time elapsed from the injection of the parcel in the domain to the first occasion the total stress experienced by the particle crosses the critical limit (Figure 2.4). This time lag is called *exit time*. From the exit time computation, for each particle one defines the breakup rate as:

$$f_{\sigma_{cr}} := \frac{1}{\langle \tau_{\sigma_{cr}} \rangle} \quad (2.15)$$

where $\langle \cdot \rangle$ is an ensemble average operator over the total number of particles. Actually, there is an important thing to take into account: the particles that were subject to a total stress exceeding the threshold already at time t_0 , i.e., at the position they were released, shall be excluded from the statistical ensemble. In fact, such breakups would be governed by the frequency of release and not by the turbulent actions of the flow. A second time scale concerning brittle rupture of particles can be introduced, that is the time lag $T_{\sigma_{cr}}$ (see, Figure 2.4), referred to as *diving time* and defined theoretically as the time interval between the last down-crossing and the first up-crossing with respect to the release time. One can then define a so-called

proxy breakup rate [4]:

$$\tilde{f}_{\sigma_{\text{cr}}} := \frac{1}{\langle T_{\sigma_{\text{cr}}} \rangle} \quad (2.16)$$

The physical scenario changes in the case of ductile breakage. Here the exit time $\tau_{\sigma_{\text{cr}}}$ does not mark the breakage of the particle. Instead, it represent the point of activation of the damaging process. Indeed, for a ductile parcel the physical process leading to rupture can be outlined as follows:

1. The particle is released at some position \mathbf{x}_0 at the initial time t_0 and starts drawing its own trajectory.
2. At some time instant it is subject to a total stress that overcomes the critical activation value σ_{cr} . This event constitutes the activation for the strain energy accumulation by the particle.
3. The particle keeps accumulating deformation energy across all time intervals for which the total stress acting on the particle is larger than the mechanical strength.
4. At the moment when the accumulated deformation energy stored by the particle surpasses the maximum admissible strain energy (which is a property of the particle itself) then the aggregate undergoes breakage.

This phenomenological description is shown in Figure 2.5. There, the red-shaded areas represents the energy-accumulation time intervals.

In the present work, the deformation energy is defined as (see [3]):

$$\mathcal{E}(t) = \int_{t_0}^t \sigma_{\text{tot}}(\mathbf{x}_p(\tau), \tau) \theta(\sigma_{\text{tot}} - \sigma_{\text{cr}}) d\tau \quad (2.17)$$

where $\theta(\cdot)$ is the Heaviside function. To measure the ductile breakup rate we refer to the breakage time, defined here as:

$$\tau(\sigma_{\text{cr}}, \mathcal{E}_{\text{cr}}) = \tau : \int_{t_0}^{\tau_{\text{cr}}} \sigma_{\text{tot}}(\mathbf{x}_p, t) \theta(\sigma_{\text{cr}} - \sigma_{\text{tot}}) dt = \mathcal{E}_{\text{cr}} \quad (2.18)$$

and then, once the breakage time has been gathered for the entire particle bundle, the ductile breakup rate is computed in the same way as in the brittle case, namely

$$f(\sigma_{\text{cr}}, \mathcal{E}_{\text{cr}}) =: \frac{1}{\langle \tau(\sigma_{\text{cr}}, \mathcal{E}_{\text{cr}}) \rangle} \quad (2.19)$$

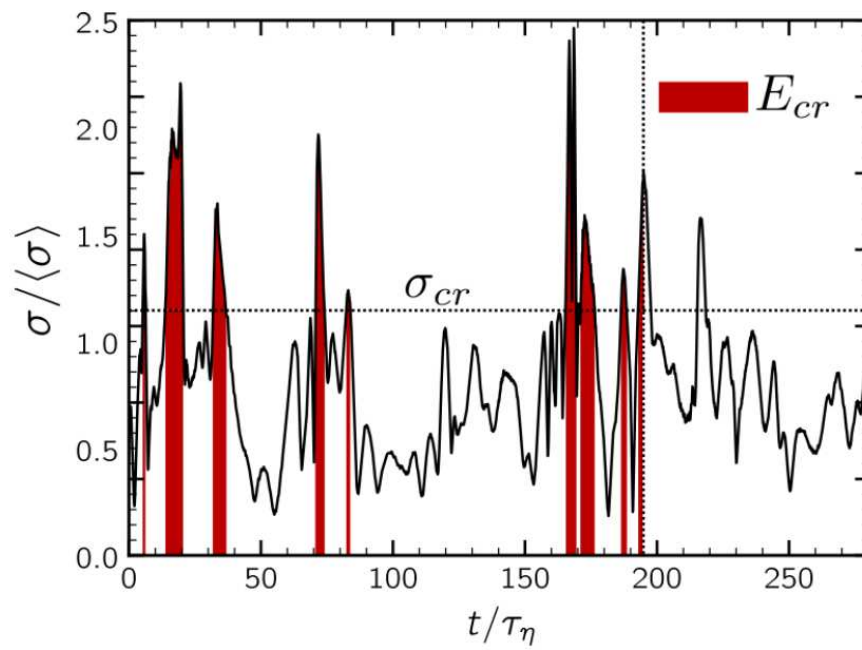


Figure 2.5: Graphical representation of the energy accumulation by the tracked particle. The particle accumulates strain energy during the time intervals where the experienced total stress exceed the stress threshold.

Chapter 3

Results and Discussion

3.1 Hydrodynamics

The findings of the hydrodynamical study of the rotating tank are reported. First, Figure 3.1 shows the convergence profiles relative to three integral quantities, namely the volume flow rate across the cross-sections of the domain (top panel), the mean value of the turbulent energy dissipation rate averaged onto three different cross-sections and into the whole domain (central panel), and the area weighted average of the wall-shear stress on the cap surface (bottom panel). The convergence of the RANS simulation can be deduced from the long invariant tail shown by all the monitored variables. Once the convergence of the simulation was reached, the first data being analyzed was the mean profiles of the tangential velocity. Figure 3.2 (left panel) shows the mean velocity profiles assessed at the mid-radius vertical lines in three different cross-sections, while the right panel displays the local velocity profiles captured at different vertical lines (different radius) defined in the same cross-section. It can be noted how the layers become more and more intense as the radius of the vertical line at which the profiles are evaluated increases. Moreover, the y -coordinate of the zero-toroidal velocity point (i.e., the intersection of the profile with the vertical line with 0 abscissa) moves upward towards the middle of the vertical line (i.e., $y = 0.010$ m) as the radius augments. This is due to the centrifugal effect which makes the tangential velocity of the fluid particles higher as they move radially. These observations confirm the a-priori hypothesis that the hot-spot for turbulent motion is exactly the zone close to the upper-outer edge (where indeed the mesh fineness has been incremented).

Then, wall-solution data have been analyzed. Figure ?? outlines the distributions of the wall y^+ (left panel) and wall-shear stress (right panel) evaluated at both the bed and cap surfaces. The y^+ behaviour yields a very nice information, that is the incredibly good level of resolution achieved ($y^+ < 0.2$ across all the domain boundaries). On the other hand, from the τ_w distributions it is evident how, on average, it is indeed the cap surface to experience the higher shear stress (the peak

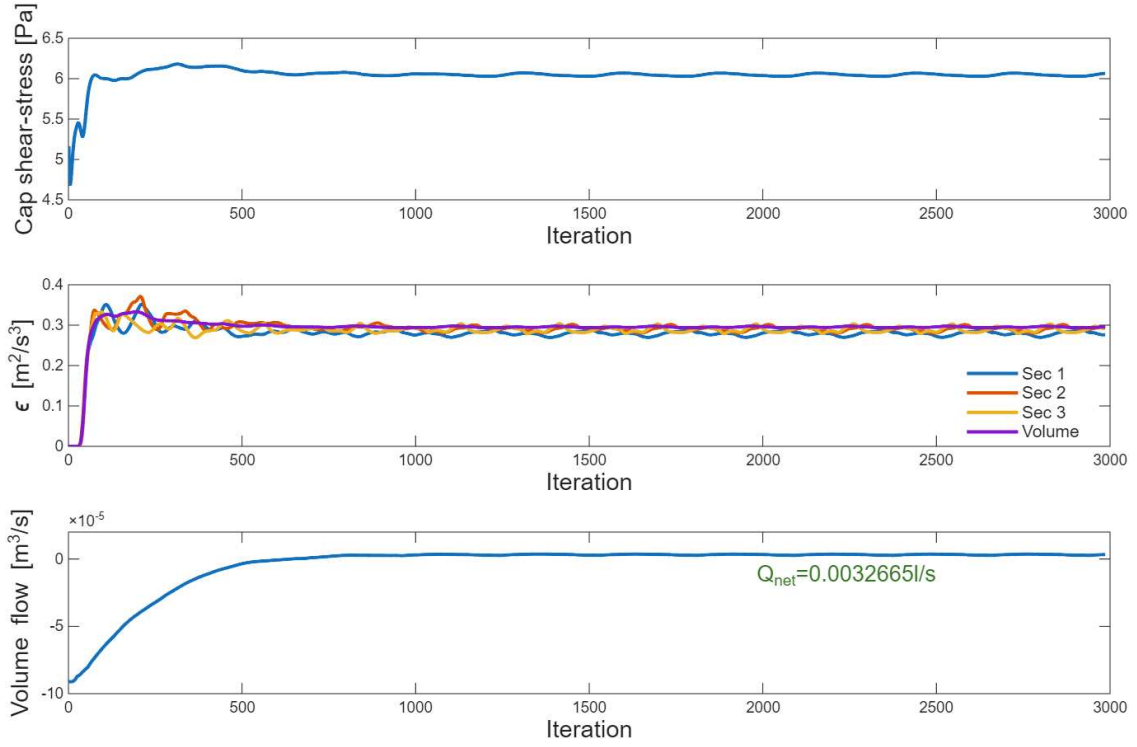


Figure 3.1: Outline of the monitored quantities utilized to establish convergence of the solution. From the long flat tail we can infer the solution was sufficiently converged.

of the τ_w distribution on the cap is approximately 26.6% higher than the peak on the bed).

Table 3.1: Characteristic flow value derived from RANS, along with mesh properties and solver time-step-size.

ν [m^2s^{-1}]	Q_{net} [ls^{-1}]	$\bar{\varepsilon}$ [m^2s^{-3}]	η [μm]	τ_η [ms]	$\bar{\ell}$ [μm]	ℓ_{min} [μm]	Δt_{LES} [ms]
$1.0048 \cdot 10^{-6}$	0.00327	0.2955	43.04	1.84	303.70	20	0.50

Table 3.1 groups some important fluid-dynamic parameters given by the RANS simulation along with characteristic values describing the fineness level of the mesh. These two kind of informations are stricly related, in particular for what concerns the subsequent LES simulation. Indeed, by comparing the mesh cell-length statistics with the smallest turbulent scale (i.e., the Kolmogorov length scale η) an a-priori estimation about the maximum resolved energy fraction can be made. Moreover, the value of the Kolmogorov time scale provides a guide for choosing an appropriate

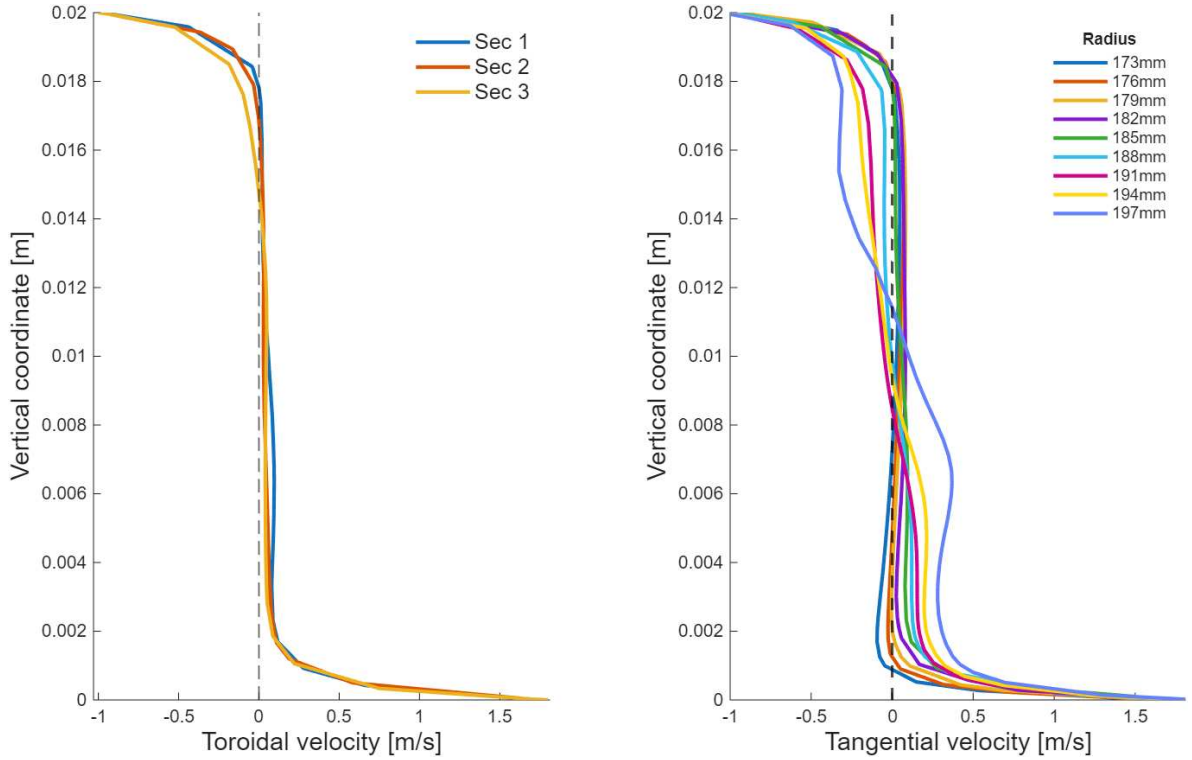


Figure 3.2: Vertical profiles of the toroidal velocity. Left panel: profiles evaluated at the mid-radius vertical line at three different cross-sections. Right panel: tangential velocity profiles at different radii.

solver time-step-size, allowing for an adequate time resolution of the large eddy dynamics. Indeed, one can see from the Table 3.1 that the selected time-step-size amounts to roughly $1/3$ of the Kolmogorov time scale. Such a value guarantees a fine temporal resolution of the resolved-eddy dynamics.

A more detailed *a-priori* discussion about the quality of the employed mesh in relation to the LES task can be made in view of Figure 3.4.

1. First of all, it should be noticed that, albeit very small, there is a fraction of cells whose characteristic length is smaller than the Kolmogorov length scale. In addition, one immediately sees that the great majority of mesh elements have a size very close to η . Thus, one can expect that the LES simulation will solve the major fraction of the energy spectrum. This is by no means obvious.
2. We employed a high-quality mesh as demonstrated by the distributions of the orthogonal quality measure and the aspect ratio. The latter shows a visible accumulation of elements pretty stretched ($AR \sim 10^2$). However, these cells belong to the inflation layer, hence were known to be excessively stretched.

Moving on toward LES simulation results, Figures 3.5 and 3.6 report the temporal

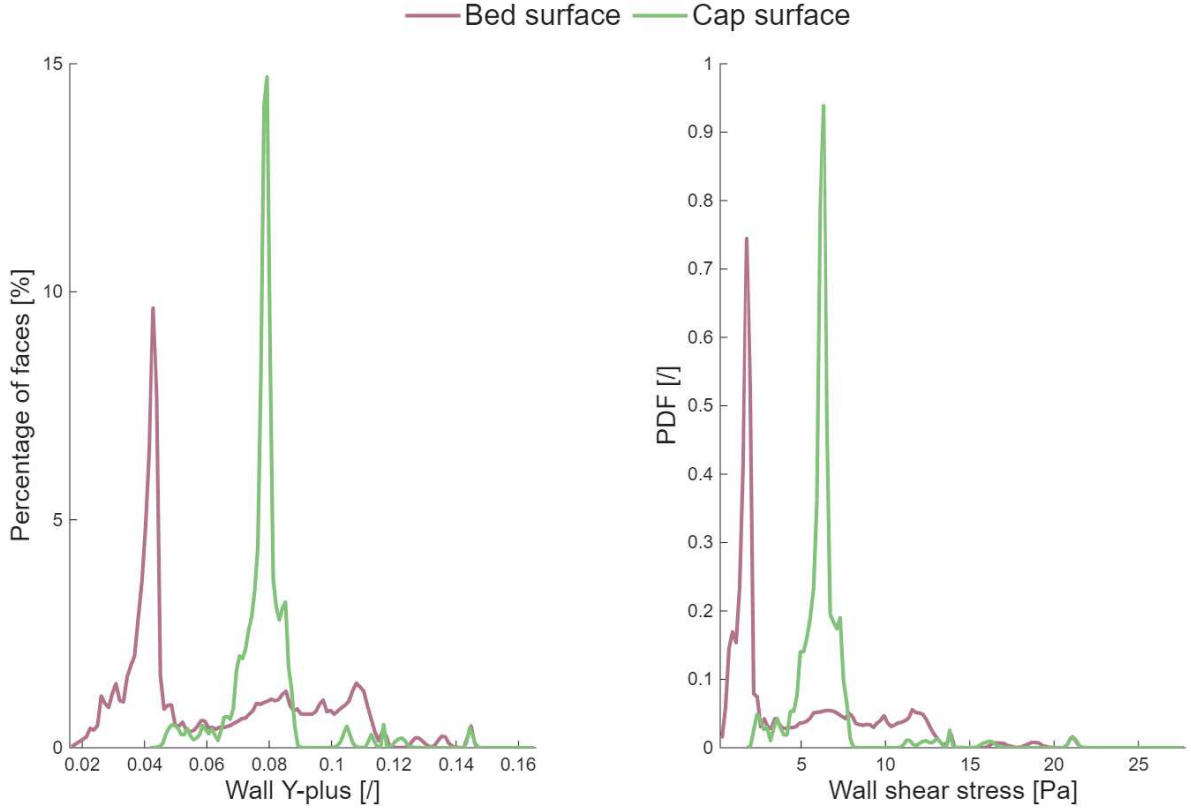


Figure 3.3: Simulated domain with named boundaries.

autocorrelation coefficients of the velocity components, along with the indication of the first zero-crossing integral scale.

The analysis of temporal correlation coefficients reveals marked differences across the monitored near-wall locations. Points characterized by shorter integral time scales lose the correlation quickly, indicating that the local velocity fluctuations are highly intermittent and dominated by rapidly evolving eddies. This behavior is consistent with regions of stronger turbulence intensity, where the decorrelation time is reduced by the continual breakdown of structures. Conversely, longer integral time scales are found in regions where coherent motions persist over extended durations, suggesting the prevalence of larger or more slowly evolving flow structures. From these considerations, it is immediate to see how the turbulence activity be noticeably higher in the identified hot-spot (which is exactly where the point upper-outer lives). A similar reasoning can be made about the toroidal autocorrelation coefficients, which are displayed in the tiled chart reported in Figure 3.7. The spatial correlation coefficients quantify the spatial extent of correlated fluctuations along the toroidal direction. Smaller integral length scales correspond to shorter correlation distances, and thus to smaller dominant eddy sizes, typically associated with near-wall turbulence. Larger values of the integral length scale indicate the

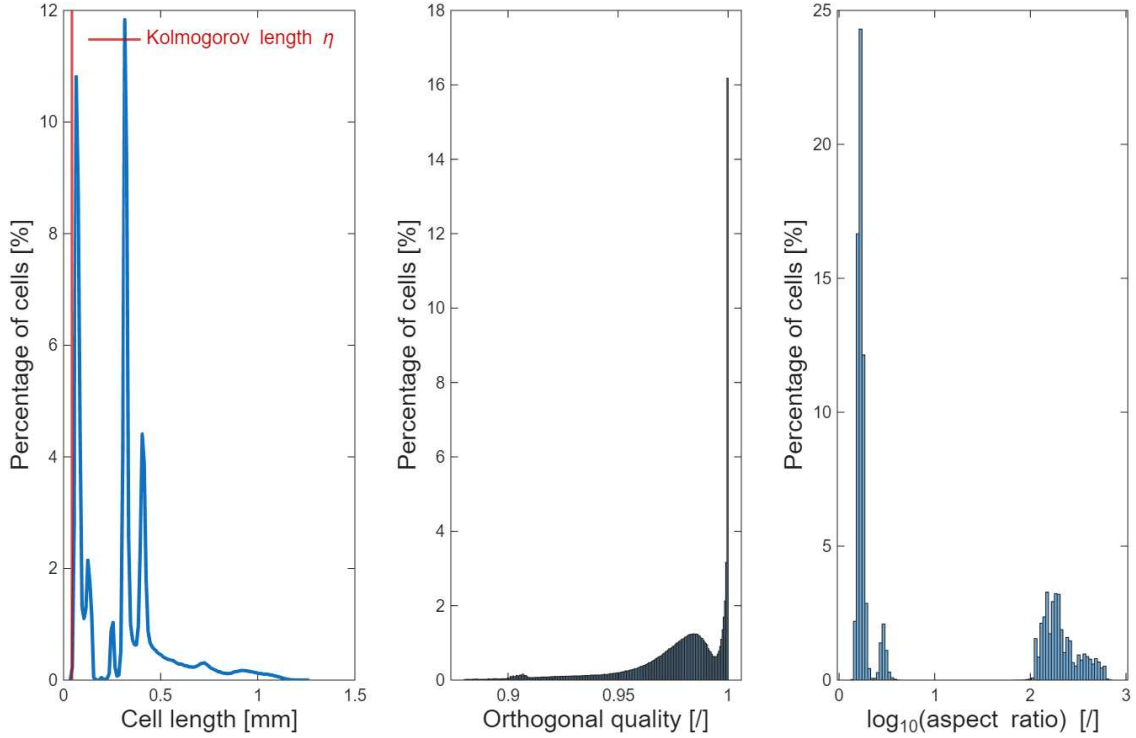


Figure 3.4: Distribution of mesh quality values. Left panel: characteristic cell length along with the indication of the Kolmogorov length scale. Central panel: orthogonal quality distribution (measure of how similar a cell is to the perfect equiangular polyhedra). Right panel: distribution of the aspect ratio (measure of over-elongation of the cells).

presence of eddies with greater spatial coherence, a feature more characteristic of the bulk flow. Together, the temporal and spatial correlation scales provide a consistent characterization of the turbulence: near-wall points are dominated by intense, small-scale and short-lived fluctuations, whereas points far from walls retain longer-lived and more spatially extended coherent structures.

Figure 3.7 shows the autocorrelation coefficients $\rho_{\theta\theta}(s)$, $\rho_{rr}(s)$ and $\rho_{zz}(s)$ of the velocity components along the longitudinal direction for the six perimetral monitoring rakes. All three autocorrelations exhibit a monotonic decay with increasing separation $s = r|\Delta\theta|$, although with markedly different correlation lengths depending on both the velocity component and the probe location. For all monitoring rake it is the streamwise velocity component (i.e., $\rho_{\theta\theta}$) that exhibit the widest integral scale ($\Lambda \approx 5 \div 22$ mm) indicating the fact that this direction is directly forced by the counter-rotating walls and then retains coherence over larger distances. Conversely, radial and vertical velocity components decorrelate much more rapidly ($\Lambda \approx 1 \div 8$), consistently with the small-scale motions in the transverse directions typical of wall-bounded flows. Among the different locations, the upper-outer region (hot-spot)

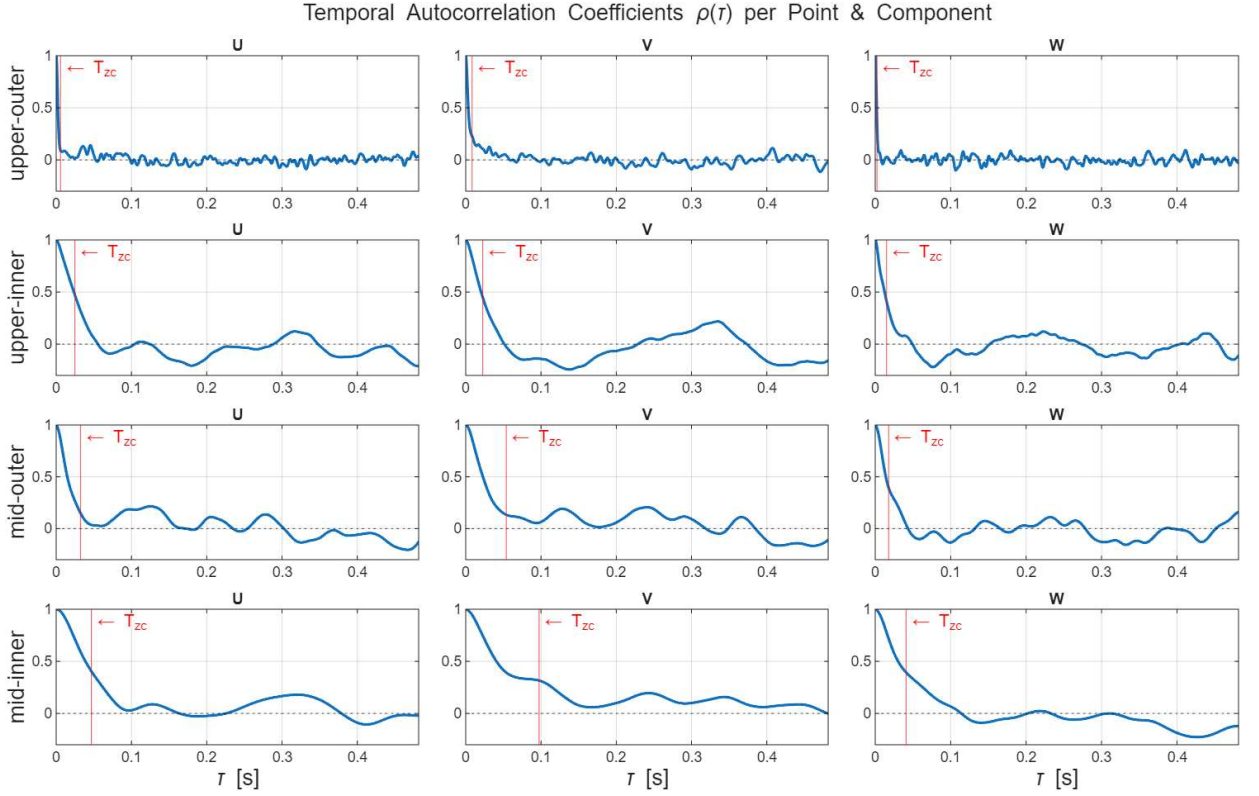


Figure 3.5: Tiled chart of temporal autocorrelation coefficients organized per monitoring point (rows) and per velocity component (columns).

exhibits the shortest correlation lengths for all components, indicating intense local turbulence production and small-scale eddies. In contrast, the lower-inner region shows the largest integral scales, particularly for the longitudinal component, suggesting the presence of smoother larger coherent structures. Overall, the hierarchy $\Lambda_{\theta\theta} \gg \Lambda_{rr} \approx \Lambda_{zz}$ is observed at all the monitoring location.

Figure 3.8 reports the cross-correlation coefficients between the velocity components (i.e., $\rho_{\theta r}(s)$, $\rho_{\theta z}(s)$ and $\rho_{rz}(s)$) along the longitudinal direction. These correlations provide insight into the coupling between different components of the fluctuating velocity field. In all cases, the strongest and most persistent correlations occur in the lower-inner region, indicating that in this part of the tank the fluctuating components are organized into larger and more coherent structures. Near the cap and outer wall, the cross-correlations are much weaker and decay rapidly, reflecting the predominance of small-scale, less organized, more chaotic turbulence. The sign of the correlations also reveals the phase relationships between components. Positive values of $\rho_{\theta z}$ indicate in-phase vertical and toroidal fluctuations, while negative lobes in $\rho_{\theta r}$ and ρ_{zr} reveal counter-motions typical of vortex tilting and secondary circulation. This behavior is consistent with the expected structure of

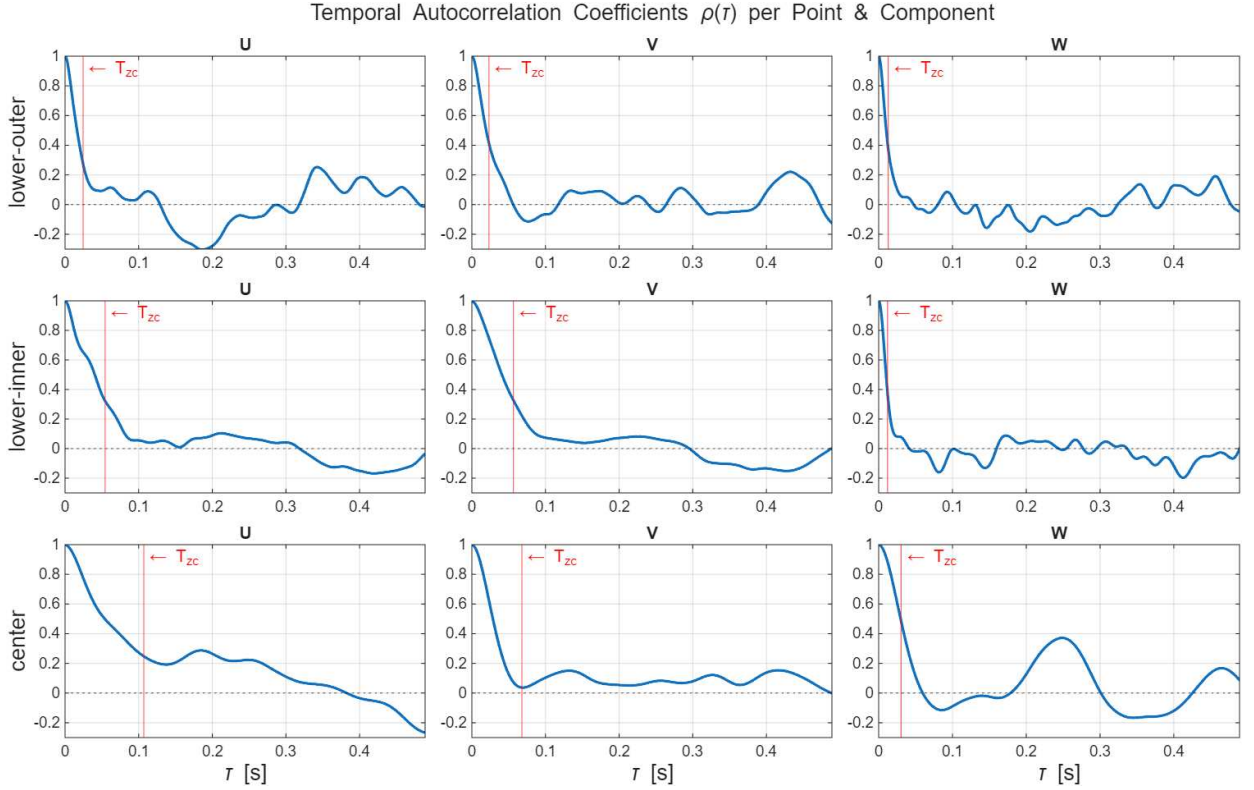


Figure 3.6: Tiled chart of temporal autocorrelation coefficients organized per monitoring point (rows) and per velocity component (columns).

wall-bounded shear turbulence, where streamwise-aligned motions persist longer than their transverse counterparts and where inter-component coupling weakens as the flow becomes more intermittent near the walls.

Figure 3.9 presents the normalized turbulent kinetic energy spectra $E(k)/\kappa$ obtained at the seven monitoring points distributed across the cross-section (upper-outer, upper-inner, mid-outer, mid-inner, lower-outer, lower-inner, and center). Normalization by the local variance emphasizes the shape of the spectral distribution, making the comparison across locations more meaningful. All spectra exhibit the expected three-region structure: an energy-containing plateau at low wavenumbers and a transition region with approximate power-law decay. However, the extent and character of these regions vary markedly with probe location. So it is worth dissecting the figure more closely:

upper-outer hotspot: The spectrum at the upper-outer point shows the richest broadband content, with a broad low- k plateau and a visible slope close to the classical $-5/3$ scaling over roughly one decade in wavenumber. This reflects the strong turbulence intensity and developed cascade generated in this shear-dominated zone.

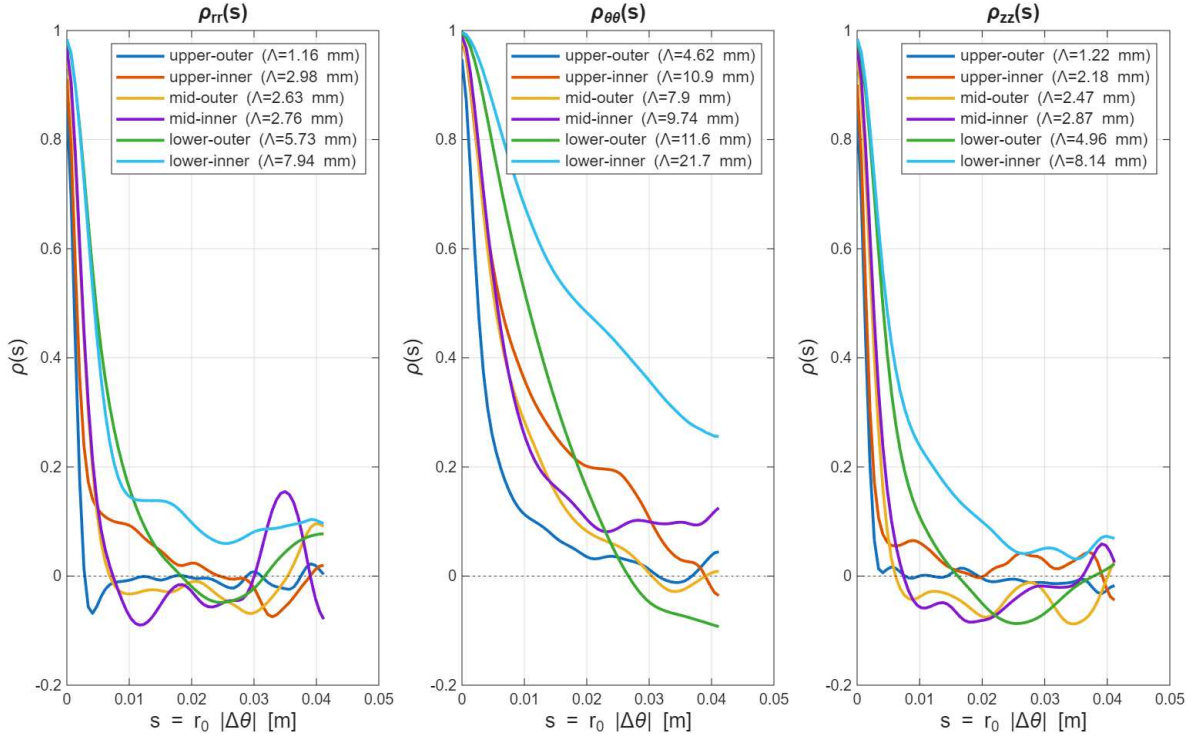


Figure 3.7: Spatial autocorrelation coefficients. Left panel: autocorrelations ρ_{rr} . Central panel: autocorrelations $\rho_{\theta\theta}$. Right panel: autocorrelations ρ_{zz} . Each panel displays the correlation coefficients of the different rakes overlaid.

Inner-wall points (upper-inner, mid-inner, lower-inner): At points closer to the inner wall, the spectra display a very rapid transition from plateau to roll-off, leaving little or no room for an inertial-like range. This indicates that turbulence in these regions is strongly constrained by the wall and dominated by local shear structures rather than a full cascade.

Mid-outer and lower-outer: These positions show intermediate behavior; a modest slope region exists, though narrower and less energetic than at the hotspot. This suggests the presence of coherent structures extending from the outer wall, but with reduced intensity away from the main shear zone.

Center: The central point exhibits the most “textbook-like” spectrum, with a broad plateau, a long and smooth power-law region, and a clean dissipative roll-off. This reflects the reduced influence of wall proximity and a more isotropic, homogeneous turbulence state in the flow core.

The spatial autocorrelations and cross-correlations consistently highlight the interplay between turbulence intensity, anisotropy, and coherence lengthscales across the domain. Regions characterized by short correlation lengths (e.g. the upper-outer

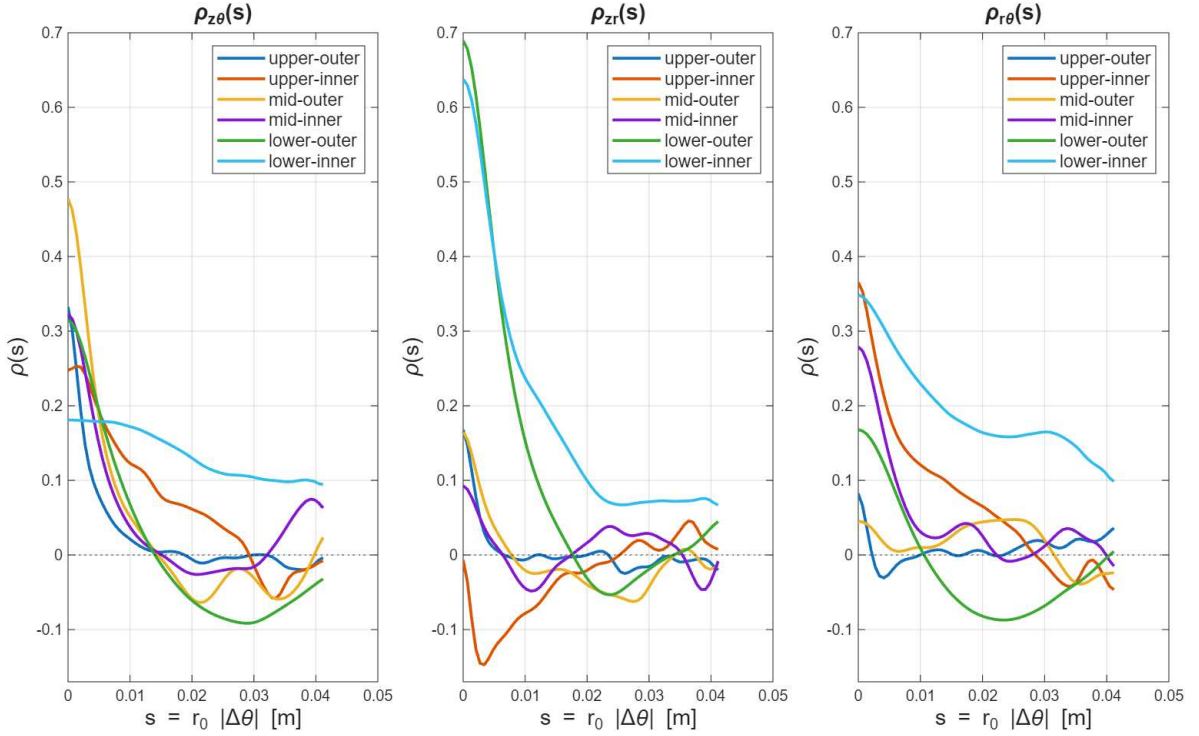


Figure 3.8: Spatial autocorrelation coefficients. Left panel: autocorrelations $\rho_{z\theta}$. Central panel: autocorrelations ρ_{zr} . Right panel: autocorrelations $\rho_{r\theta}$. Each panel displays the correlation coefficients of the different rakes overlaid.

probe near the cap) also exhibited steeper and noisier energy spectra, consistent with the dominance of small-scale turbulent fluctuations. Conversely, in the lower-inner region, where the integral scales were largest and cross-component couplings most persistent, the energy spectra revealed broader inertial subranges with a closer approach to the classical $-5/3$ law. Taken together, these results demonstrate a clear correspondence between correlation-based lengthscale estimates and spectral energy distributions, providing a coherent picture of how local turbulence structure varies across the flow domain and ultimately influences transport and mixing processes.

Finally, let us analyze the particle dynamics. Figure 3.10 represents the comparison of the shear, drag and total stress between the two particles cluster analyzed (namely $D_p = 300$ mm and $D_p = 600$ mm) along with the outline of the distribution of the relative velocity norm. We can see from the figure that the larger particles experiences larger velocity deviations with respect to the fluid. However, due this is balanced by the smaller area onto which the drag force is acting, resulting on a drag stress which is slightly higher in the 300 mm case. Concerning the turbulent shear stress, we notice a similar trend for both the particle families, apart for the right tail, where it is evident that the smaller particles on average experience large bursts of stress with definitely higher frequency with respect to the larger aggregates. This

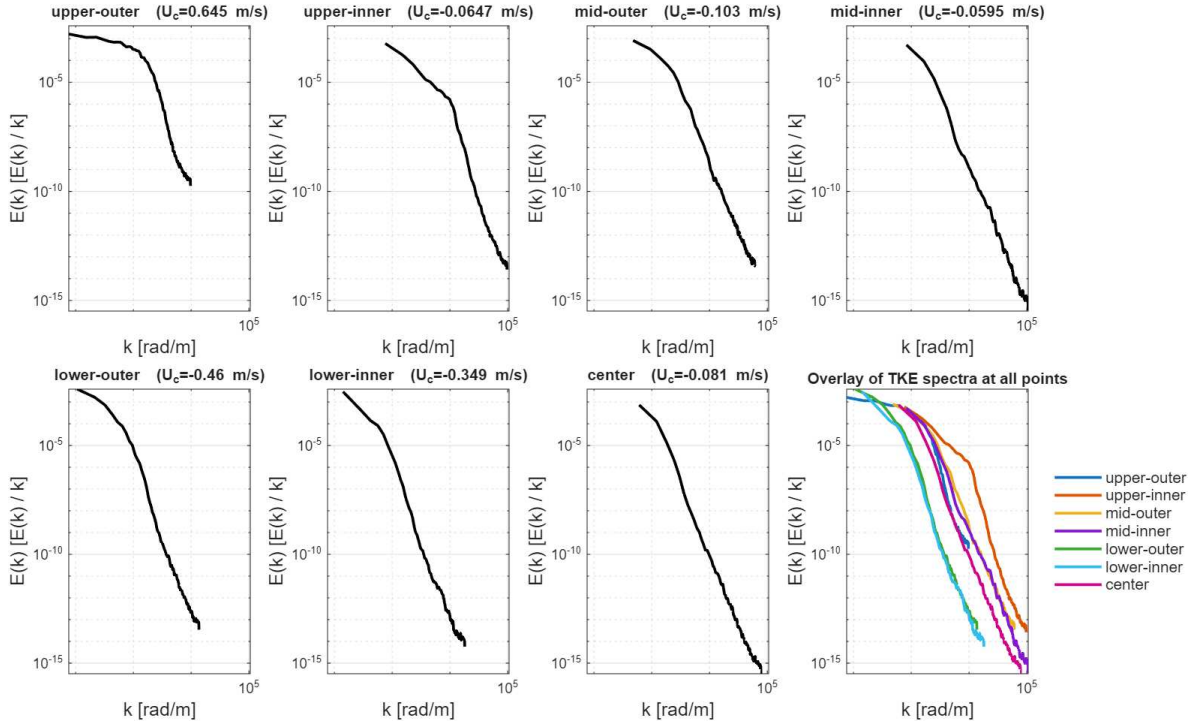


Figure 3.9: Tiled layout of turbulent energy spectra. The different panels represent the turbulent kinetic energy spectra normalized by the turbulent kinetic energy value (to better compare the shapes) for the 7 different monitored near-wall plus center points. Bottom-right panel reports all the spectra overlaid.

is probably due to the trapping effect of the smaller particles in the hot-spot zone, which is undoubtedly much more relevant for the small size case. Indeed, due to the higher relative velocities by which they are characterized, the larger particles can escape segregation with much more facility. Finally, one can see that for the present case it is the turbulent shear stress that prevail over the drag effect, causing a higher probability for the small-size particle to be subjected to intense loading events.

Figure 3.12 reports the breakup rate in the brittle case for the two tested particle clusters. As one can see, the breakup rate is in general higher for the larger-size particles. The difference between the rates is more marked for low values of the threshold stress. For small values of the critical stress, can expect a similar behaviour for the ductile breakup rates, since, as displayed in Figure 3.12, even if the smaller particles accumulate slightly higher values of energy, the probability of these events is too low to expect statistical incidence. Conversely, as the value of the critical stress augments, the smaller particles are able to store markedly higher values of energy with ever increasing probability. Consequently, We can expect a trend inversion for large values of the activation threshold.

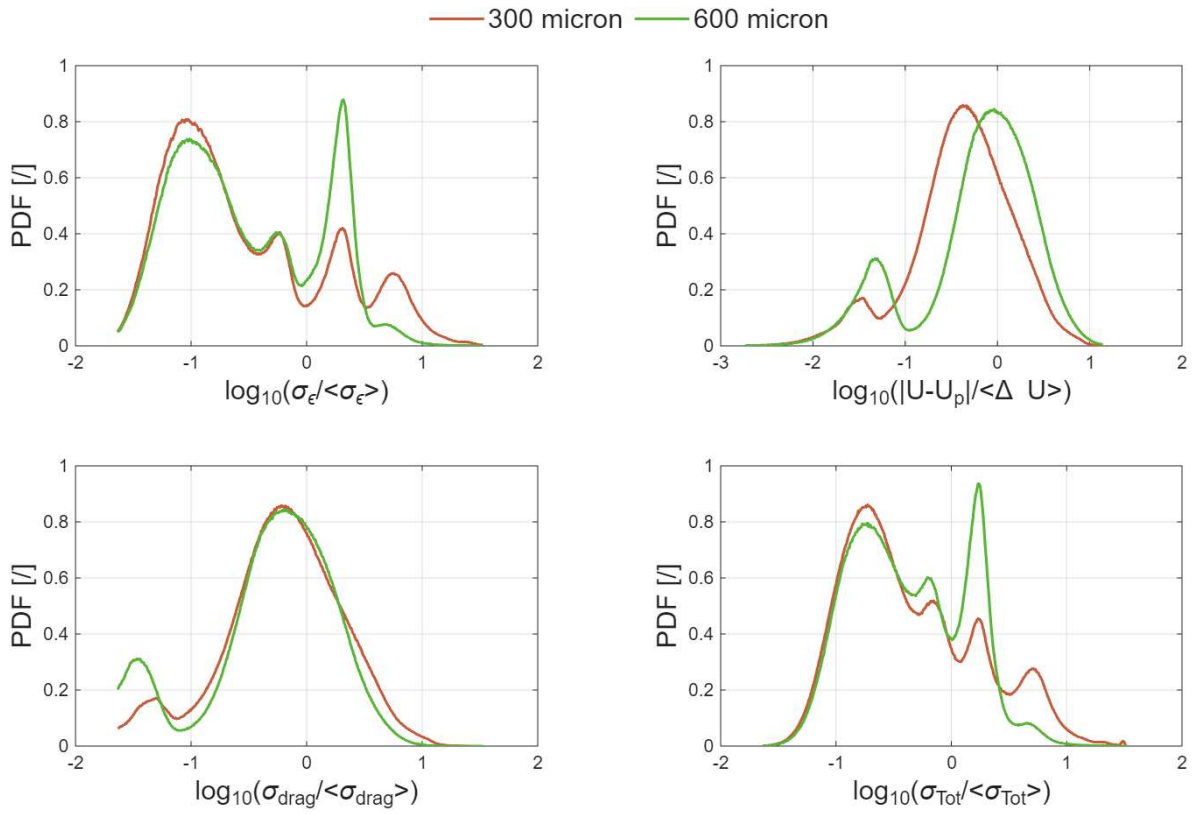


Figure 3.10: Comparison of particles stress distributions for the two tested particle clusters. Upper-left panel: distribution of the turbulent shear stress normalized by the overall mean shear stress experienced. Upper-right panel: distribution of the relative velocity between particles and fluid phase, normalized by the mean drift velocity. Bottom-left panel: distribution of the drag stress normalized by the mean drag stress felt by the tested clusters. Bottom-right panel: distributions of the total stress experienced by the particles normalized by its mean value.

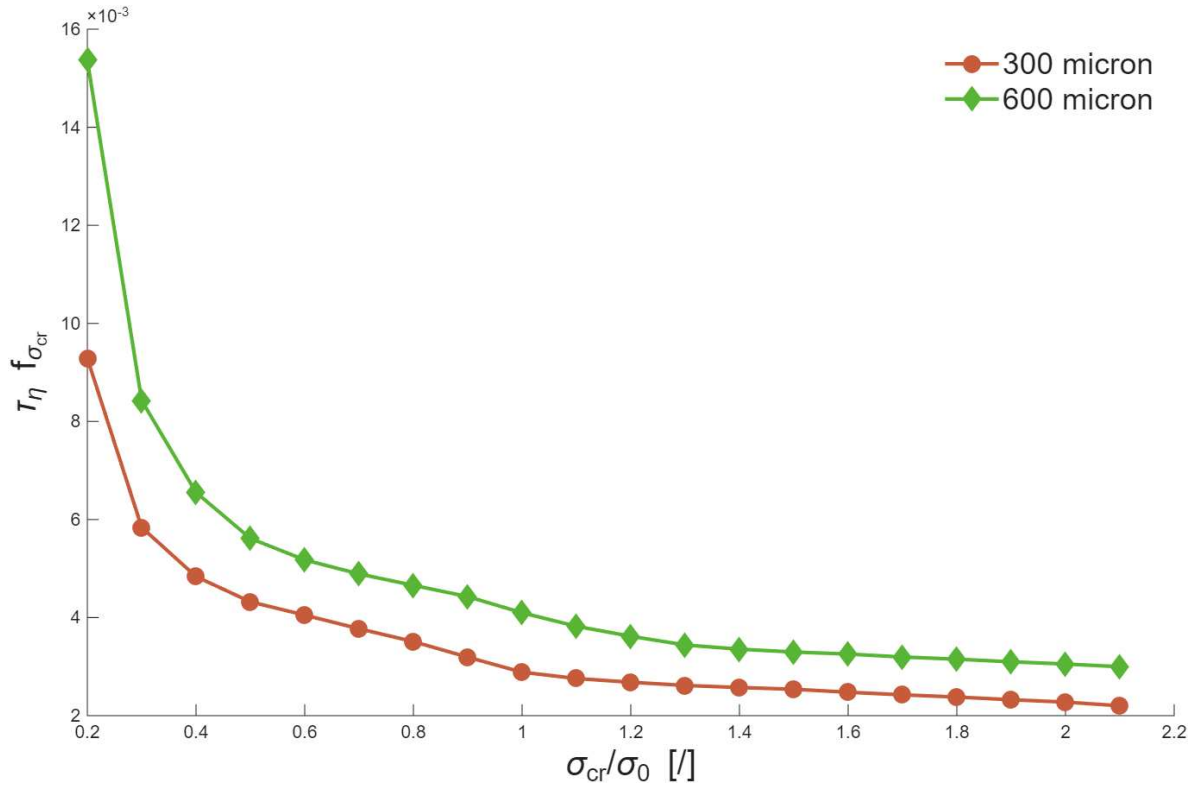


Figure 3.11: Outline of the breakup rates for the two particle clusters. The x -axis reports the value of the adopted critical stress threshold, normalized by the mean total stress. The y -axis reports the particle breakup rate, normalized by the Kolmogorov time scale τ_η .

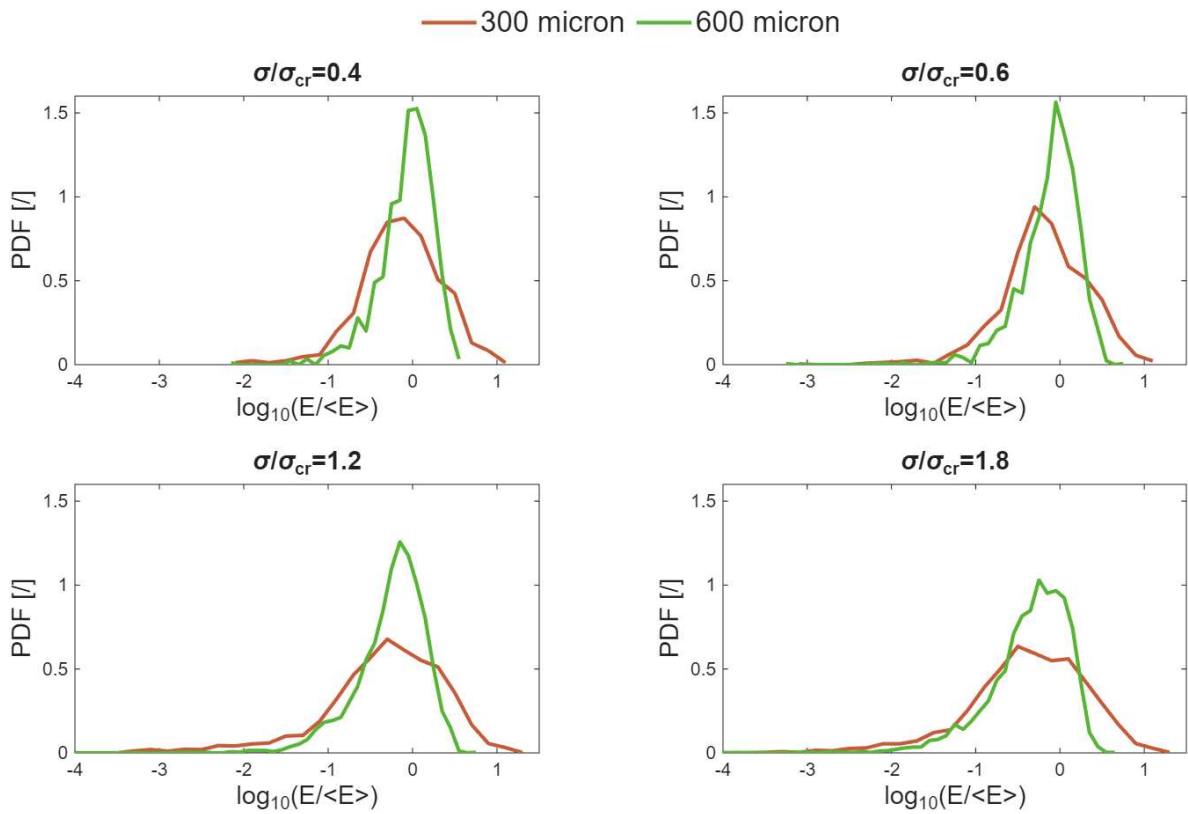


Figure 3.12: Comparison of the accumulated strain energy for the two tested particles clusters at varying values of the activation stress σ_{cr}

Appendix A

Some Background

A.1 Hydrodynamics

In general, it is well-known that the dynamics of a Newtonian compressible fluid flow is governed by the *Navier-Stokes equations*. These are, in the general case, a set of nonlinear unsteady partial differential equations and in a Cartesian reference frame $Ox_1x_2x_3$ write as:

$$\frac{\partial \rho}{\partial t} + \frac{\partial}{\partial x_j}(\rho u_j) = 0 \quad (\text{A.1})$$

$$\frac{\partial}{\partial t}(\rho u_i) + \frac{\partial}{\partial x_j}(\rho u_i u_j) = -\frac{\partial p}{\partial x_i} + \frac{\partial}{\partial x_j} \left(\mu S_{ij} - \frac{2}{3} \frac{\partial u_k}{\partial x_k} \delta_{ij} \right) \quad (\text{A.2})$$

where $\mathbf{u} = (u_i)_{i=1,2,3}$ is the (Eulerian) velocity vector field, $p = p(\mathbf{x}, t)$ is the hydrostatic pressure field and $S_{ij} = 1/2(\partial_i u_j + \partial_j u_i)$ is the rate-of-strain tensor (i.e., the symmetric part of the velocity gradient). These fundamental conservation equations must be satisfied *instant-wise and point-wise* throughout the dynamics of the system. Since a closed-form analytical solution of the NS equations has not been found out yet (in fact we still do not know if such exists and, in case, it is unique), one has hitherto tackle them numerically. First of all, in the simpler scenario where the flow is *incompressible* (for instance, when the operating fluid is a liquid and the heat transfer which the system is subject to is negligible), then equations (A.2) simplify to:

$$\begin{aligned} \frac{\partial u_i}{\partial x_i} &= 0 \\ \frac{\partial u_i}{\partial t} + \frac{\partial}{\partial x_j}(u_i u_j) &= -\frac{\partial p}{\partial x_i} + \nu \frac{\partial^2 u_i}{\partial x_i^2} \end{aligned} \quad (\text{A.3})$$

Equations (A.3) implicitly assumed that the heat exchanges taking place in the fluid dynamics are negligibly small, so that the molecular viscosity is allowed to be considered constant and can hence taken outside the derivative operator.

As already said above, the NS equations are the fundamental governing laws for each “flow problem”, being it *laminar* or *turbulent*. The one just introduced is one of the basic characterization of fluid flows. It can be said that:

Laminar flow: said in a joke they are the calm motions of fluids. The kind of fluid, domain and dynamics characteristics are such that the fluid streams in such a way that layers of fluid slide on to each other. They are the easiest kind of flows to model and in fact for several laminar flow configurations analytical solutions to NS do exist.

Turbulent motion: gathering this definition from [kundu], we can define *turbulence* as a dissipative flow state characterized by nonlinear fluctuating three-dimensional vorticity. If we had to associate turbulence with some descriptive flags then these would hands-down be *fluctuations, nonlinearity, vorticity, dissipation, diffusivity*.

Given a flow problem, one can assess if this is a laminar flow or a turbulent flow based on the value taken on by the characteristic *Reynolds number*, defined as

$$\text{Re} = \frac{\rho UL}{\mu} \tag{A.4}$$

where U and L are the velocity and lengthscale, respectively, of the flow configuration at hand. In fact, from a physical viewpoint the Reynolds number represent the ratio between the *inertial forces* and the *viscous forces* acting on a fluid element. If Re is low, then the effects of viscosity prevail over inertial ones, and hence as a direct consequence all instabilities, fluctuations and disturbances are smeared out by viscosity, leading to a condition of regular, unperturbed (i.e., laminar) flow. As the value of Reynolds number increases, then the contribution of viscous effect starts to get uneffective, therefore every (inevitable) instability source happens to propagate and grow throughout the domain: the flow is *transitioning* towards a turbulent character. Then, for very high values of Re , the inertial effects are so intense that perturbations grow unpredictably, flow variable at each point in the domain vary chaotically in time, the motion is fully three-dimensional with an important fluid transport also in the directions orthogonal to the streamwise one. The flow is pervaded by vortical structures that swirl and and transported themselves by the flow, undergoing rupture in smaller and smaller whorls that spiral faster and faster. This flow condition is, indeed, the fully turbulent motion. The modern theorization of turbulence was first conceived by *Kolmogorov*, who devised the famous and prominent concept of *energy cascade* according to which the vortical structures, or *eddies*, acquire energy from the mean flow with which they interact. Such eddies, then, undergo rupture in smaller eddies which swirl faster and to which they feed energy, and this process keeps going until the scale

of the whorls is so tiny that molecular viscosity effects become predominant and energy is dissipated into heat.

When studying turbulent flows, there are basically three approaches that one can follow in order to address the problem: the first strategy goes under the name of Direct Numerical Simulation (DNS). In this approach one aims at resolving the whole turbulent length and timescales, revealing the dynamics of the smallest dissipative eddies, without introducing any modeling. It is an approach that, to date, is doable solely for very simple academic flow domains at not-too-high Reynolds numbers, due to the extremely tiny mesh sizes and time-step-sizes necessary to describe the dynamics at the smallest scales. Absolutely hitherto inapplicable to real engineering flow scenario. Conceptually opposite with respect to the DNS is the Reynolds-Averaged Navier-Stokes (RANS) equations approach. In this case, one is uniquely interested in resolving the dynamics of the mean flow, without assessing the vortical dynamics at any scales. The turbulence dynamical effect is here modeled through the addition of one or more transport equations that complement the NS equation. In the middle between DNS and RANS lies a third approach, referred to as Large Eddy Simulation (LES). This strategy starts by the consideration that are the larger eddies to carry the majority of the energy budget. Moreover, at the smallest dissipative scales the turbulence shows a sort of universality and, in addition, turns out to be homogeneous and isotropic, as firstly pointed out by Kolmogorov ([...]). Thus, it is reasonable to resolve not the entire range of scales, but only the fraction relative to the macro-eddies. Conversely, the dynamics of the micro-eddies is modeled (this is why LES approach is conceptually the encounter point between RANS and DNS).

RANS Simulations

The first thing to note is that the flow variables (velocity components, pressure, temperature, ...) at each point in the domain can be written as the superposition of a contribution due to the mean flow (represented by a capital letter or an overbar), plus a contribution (the noisy chaotic one) related to the passage of the vortical unpredictable structures (represented with a prime symbol). This one is called *Reynolds decomposition* and, taking as an example a velocity component v , writes as:

$$v = V + v' , \quad V \equiv \langle v \rangle , \quad v' \equiv v - V \tag{A.5}$$

where $\langle \cdot \rangle$ represent an averaging process (see [...] for an insight on the different averaging procedures). Then, by applying the averaging operator to the whole NS equations, after some computation and rearrangement one ends up with the

prominent *RANS equations*, which for an incompressible adiabatic flow write as:

$$\frac{\partial U_i}{\partial x_i} = 0 \quad (\text{A.6})$$

$$\frac{\partial U_i}{\partial t} + \frac{\partial}{\partial x_j}(U_i U_j) = \frac{1}{\rho} \frac{\partial}{\partial x_j}(-P \delta_{ij} + 2\mu \bar{S}_{ij} - \rho \overline{u_i u_j}) \quad (\text{A.7})$$

where $\bar{S}_{ij} = 1/2(\partial_i U_j + \partial_j U_i)$ is the mean rate-of-strain tensor. It is worth noting that the RANS equations are formally identical to the instantaneous NS equations, except for one term in the stress tensor which has compared after the averaging process, namely $-\rho \overline{u_i u_j}$. Such a new term is referred to as *Reynolds stress tensor*, and unfortunately the process of average has not provided any supplementary equation to compute it. The problem of assessing the Reynolds stress tensor is known as the *closure problem* and it give rise to the world of turbulence models.

LES Simulations

The governing equations being addressed in a LES simulation are obtained by *filtering* the time-dependent NS equations. The filtering operation in fact filters out the eddies that are smaller than the filter width, and therefore the resulting equations govern the dynamics of the large eddies. A filter is nothing but an integral operator applied to the flow variables. Thus, for a given variable ϕ , the its filtered counterpart will be:

$$\bar{\phi}(\mathbf{x}) = \int_D G(\mathbf{x}, \mathbf{x}') \phi(\mathbf{x}') d\mathbf{x}' \quad (\text{A.8})$$

where D is the fluid domain, and $G(\cdot, \cdot)$ is the filter function. After the process of filtering the time-dependent NS equations, we obtain the LES governing equations that write as:

$$\begin{aligned} \frac{\partial \rho}{\partial t} + \frac{\partial}{\partial x_i}(\rho \bar{u}_i) &= 0 \\ \frac{\partial}{\partial t}(\rho \bar{u}_i) + \frac{\partial}{\partial x_j}(\rho \bar{u}_i \bar{u}_j) &= \frac{\partial}{\partial x_j} \left(-\bar{p} \delta_{ij} + 2\mu \bar{S}_{ij} - \tau_{ij} \right) \end{aligned} \quad (\text{A.9})$$

where $\bar{S}_{ij} = 1/2(\partial_i \bar{u}_j + \partial_j \bar{u}_i)$ is the filtered rate-of-strain tensor whereas τ_{ij} is the subgrid-scale stress defined as:

$$\tau_{ij} = \rho(\overline{u_i u_j} - \bar{u}_i \bar{u}_j) \quad (\text{A.10})$$

Bibliography

- [1] Rosetta blackman et al. “Environmental DNA: The next chapter”. In: *Molecular Ecology* (2024).
- [2] Jelle A Dercksen et al. “The Impact of Flow Velocity on Environmental DNA Detectability for the Application in River Systems”. In: *Environmental DNA* (2025).
- [3] Graziano Frungieri et al. “Ductile Breakup of Tracer Aggregates in Homogenous Isotropic Turbulence”. In: *Chemical Engineering Transactions* (2023).
- [4] Graziano Frungieri et al. “Heavy and light inertial particle aggregates in homogeneous isotropic turbulence: A study on breakup and stress statistics”. In: *Computers and Fluids* (2023).
- [5] K A Kusters. “The Influence of Turbulence on Aggregation of Small Particles in Agitated Vessels”. PhD Thesis. Technische Universiteit Eindhoven, 1991.